Zitierweise: *Angew. Chem. Int. Ed.* **2020**, *59*, 11634–11640
Internationale Ausgabe: doi.org/10.1002/anie.202004562
Deutsche Ausgabe: doi.org/10.1002/ange.202004562

Photoluminescence

Incorporating Rare-Earth Terbium(III) Ions into $Cs_2AgInCl_6$:Bi Nanocrystals toward Tunable Photoluminescence

*Ying Liu[+], Ximing Rong[+], Mingze Li, Maxim S. Molokeev, Jing Zhao und Zhiguo Xia**

Abstract: *The incorporation of impurity ions or doping is a promising method for controlling the electronic and optical properties and the structural stability of halide perovskite nanocrystals (NCs). Herein, we establish relationships between rare-earth ions doping and intrinsic emission of lead-free double perovskite $Cs_2AgInCl_6$ NCs to impart and tune the optical performances in the visible light region. Tb^{3+} ions were incorporated into $Cs_2AgInCl_6$ NCs and occupied In^{3+} sites as verified by both crystallographic analyses and first-principles calculations. Trace amounts of Bi doping endowed the characteristic emission ($^5D_4 \rightarrow {}^7F_{6\text{-}3}$) of Tb^{3+} ions with a new excitation peak at 368 nm rather than the single characteristic excitation at 290 nm of Tb^{3+}. By controlling Tb^{3+} ions concentration, the emission colors of Bi-doped $Cs_2Ag(In_{1-x}Tb_x)Cl_6$ NCs could be continuously tuned from green to orange, through the efficient energy-transfer channel from self-trapped excitons to Tb^{3+} ions. Our study provides the salient features of the material design of lead-free perovskite NCs and to expand their luminescence applications.*

Introduction

Lead-free halide perovskite nanocrystals (NCs) have attracted intense research efforts recently as possible alternatives to lead-halide perovskite NCs to address the ambient instability and lead toxicity issues of such compounds for the realization of industrial development.[1] Several classes of related materials that replace lead with other elements have been explored.[2] Isovalent substitution of Pb^{2+} with less-toxic Sn^{2+} or Ge^{2+} is a straightforward method. Unfortunately, the resulting compounds $CsBX_3$ ($B = Sn^{2+}$ and Ge^{2+}) exhibit poorer stabilities than lead-halide perovskites ascribed to the easy oxidations of Sn^{2+} and Ge^{2+} to their corresponding 4+ states.[3] Another important alternative approach to replacing two Pb^{2+} ions with one monovalent (M′) and one trivalent (M″) cation to form the M′ and M″ octahedra, obtaining a $A_2M'M''X_6$ three dimensional (3D) double perovskite structure. Theoretically, in the generic chemical formula $A_2M'M''X_6$, M′ could be Ag^+, Na^+, Cu^+ and M″ could be Bi^{3+}, Sb^{3+}, In^{3+} to form many possible compositions.[4] Experimentally, Cs_2AgBiX_6, $Cs_2AgInCl_6$, $Cs_2AgSbCl_6$, $Cs_2NaBiCl_6$ and their alloys have been synthesized as colloidal NCs.[5] However, most air-stable double perovskite NCs have either large band gaps or forbidden optical transitions,[6] leaving the challenges in realizing optoelectronic applications and thus motivating researchers to develop strategies to improve the optoelectronic properties.[7]

Lanthanide (rare earth) ion incorporation or doping is considered a promising approach to imparting and tailoring the optical and optoelectronic performances of inorganic materials over the visible and near infrared region. The lanthanide ions (Ln^{3+}) usually exhibit unique emissions with sharp spectral linewidths compared with transition metal ions whose emissions are relatively broadband. Ln^{3+} ions prefer locating in sites with a coordination environment CN ≥ 6 (CN = coordination number). Lead-free double perovskites and lead halide perovskites provide octahedral coordination (CN = 6) for the B-site cation and M″-site cation, respectively, thus making them ideal hosts for lanthanide-ion incorporation.[8] For lead-halide perovskite NCs, different lanthanide ions have been successfully doped into the lattice for imparting optical functionality or improving the stability of NCs.[9] However, to our knowledge, only several successful examples of Ln^{3+} ions doping into the lead-free perovskite

[*] Y. Liu,[+] M. Z. Li, Prof. J. Zhao, Prof. Z. G. Xia
The Beijing Municipal Key Laboratory of New Energy Materials and Technologies, School of Materials Sciences and Engineering, University of Science and Technology Beijing
Beijing 100083 (P. R. China)
E-Mail: xiazg@ustb.edu.cn
Dr. X. M. Rong[+]
Shenzhen Key Laboratory of Special Functional Materials, Shenzhen Engineering Laboratory for Advanced Technology of Ceramics, Guangdong Research Center for Interfacial Engineering of Functional Materials, College of Materials Science and Engineering, Shenzhen University
Shenzhen 518060 (P. R. China)
Prof. M. S. Molokeev
Laboratory of Crystal Physics, Kirensky Institute of Physics, Federal Research Center KSC SB RASs
Krasnoyarsk 660036 (Russia)
and
Department of Engineering Physics and Radioelectronics, Siberian Federal University
Krasnoyarsk 660041 (Russia)
and
Department of Physics, Far Eastern State Transport University
Khabarovsk 680021 (Russia)
Prof. Z. G. Xia
The State Key Laboratory of Luminescent Materials and Devices, Guangdong Provincial Key Laboratory of Fiber Laser Materials and Applied Techniques, School of Materials Science and Technology, South China University of Technology
Guangzhou 510641 (P. R. China)
E-Mail: xiazg@scut.edu.cn
[+] These authors contributed equally to this work.
Supporting information and the ORCID identification number(s) for the author(s) of this article can be found under: https://doi.org/10.1002/anie.202004562.

NCs were reported so far, mostly in the near infrared region. For example, Yb^{3+} or Er^{3+} ions doping into $Cs_2AgInCl_6$ NCs was explored by Kim's and Nag's group;[10] Chen et al. doped Yb^{3+} and Mn^{2+} ions into Cs_2AgBiX_6 NCs;[11] Tang's group doped Ho^{3+} ions into $Cs_2AgNaInCl_6$ NCs;[12] Song et al. reported Eu^{3+}-doped $Cs_3Bi_2Br_9$ quantum dots for Cu^{2+} detection.[13] Inspired by the studies described above, it is valuable to unveil new Ln^{3+} ions doping effects on lead-free double perovskite NCs and impart the optical properties in the visible range.

Herein, we incorporated Tb^{3+} ions into lead-free double perovskite $Cs_2AgInCl_6$ NCs, simultaneously preserving the consistent crystal structure and uniform cubic morphology, to impart and tune the photoluminescence (PL) performances. Accordingly, the Tb^{3+} ions site occupation was verified from experimental analyses and first-principles calculations. More importantly, Bi^{3+} ions doping in $Cs_2AgInCl_6$ NCs adjusted the excitation of Tb^{3+} ions emission to 368 nm and variation of Tb^{3+} ions doping concentration achieved tunable emission colors from green to orange. Moreover, we explored the emission mechanism and further proposed the efficient energy transfer channel with 368 nm excitation from self-trapped excitons (STEs) to Tb^{3+} ions in Bi doped $Cs_2Ag(In_{1-x}Tb_x)Cl_6$ NCs. Our study provides insights to dope Ln^{3+} ions into the lead-free double perovskite NCs to generate multiple emissions and to expand their potential as optoelectronic materials.

Results and Discussion

All samples were synthesized via a high temperature hot injection method as reported in our previous work.[14] To clarify whether the rare earth Tb^{3+} ion is doped into the $Cs_2AgInCl_6$:Bi, XRD patterns of the as-prepared Bi doped $Cs_2Ag(In_{1-x}Tb_x)Cl_6$ NCs with different Tb^{3+} concentrations x of 0, 8.3%, 14.9%, 17.1% were firstly analyzed as shown in Figure 1. All the NCs possessed the same cubic phase with no impurity detected and slight shifts of the diffraction peak of (022) plane toward smaller angle were observed for the doped samples (Figure 1a). The amounts of Tb^{3+} ions and In^{3+} ions included in the nanocrystals were ascertained by the inductively coupled plasma (ICP) measurement (Table S1 and S2 in the Supporting Information), which provided an approximately 2% Bi/In ratio. Figure 1b,c show Rietveld refinement of the XRD patterns of $Cs_2AgInCl_6$:Bi and $Cs_2Ag(In_{82.9\%}Tb_{17.1\%})Cl_6$:Bi (corresponding to Tb/In = 0.206) nanocrystals. All the peaks were indexed by cubic cell $(Fm\bar{3}m)$ with parameters close to the bulk $Cs_2Ag(In_{82.9\%}Tb_{17.1\%})Cl_6$.[15] Therefore, this structure was taken as the starting model for Rietveld refinement performed using TOPAS 4.2. Refinements were stable and gave low R-factors (Table S3, Figure 1b,c). Coordinates of atoms and main bond lengths were present in Table S4 and Table S5, respectively. Corresponding to the peak shift in Figure 1a, the cell volume $V(x)$ increased with Tb^{3+} ions doping concentrations x as shown in Figure 1d. Considering that the ionic radii $r(Tb^{3+}, CN = 6) = 0.923$ Å is smaller than $r(Cs^{+}, CN = 12) = 1.88$ Å and $r(Ag^{+}, CN = 6) = 1.15$ Å, Tb^{3+} ions should not locate in Cs and Ag sites. Only the ionic radii $r(In^{3+}, CN = 6) = 0.8$ Å is smaller than that of Tb^{3+} ions, which verifies that the partial Tb^{3+} ions are incorporated into the lattice of $Cs_2AgInCl_6$ NCs and substitute partial In^{3+} ions.

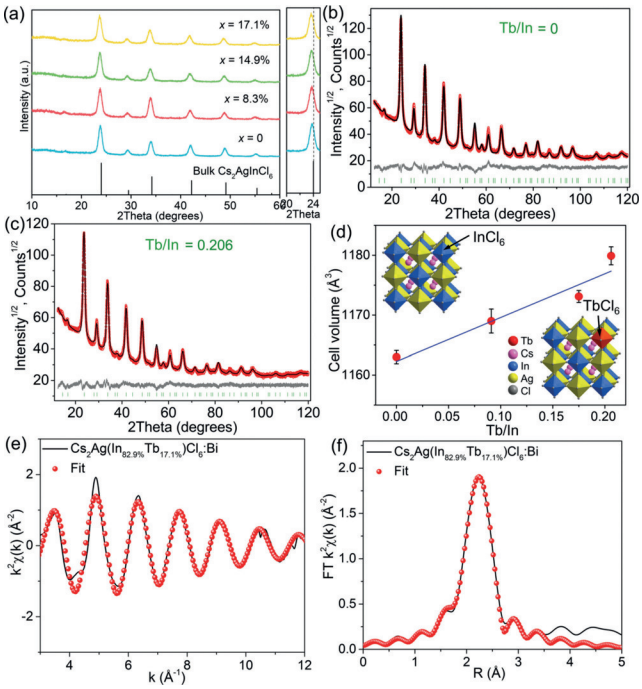

Figure 1. a) XRD patterns of Bi doped $Cs_2Ag(In_{1-x}Tb_x)Cl_6$ ($x = 0$, 8.3%, 14.9%, 17.1%) (left) and magnified XRD patterns in the approximate range of 20–25° (right). b),c) Rietveld refinement of XRD patterns for $Cs_2AgInCl_6$:Bi and Tb^{3+}-doped $Cs_2AgInCl_6$:Bi with Tb/In = 0 and 0.206, respectively. d) Variation of cell volume as a function of the value of Tb/In. Insets show the schematic of corresponding crystal structure with Tb^{3+} ions doping. e) k^2-weighted Tb L_3-edge EXAFS spectrum and f) corresponding Fourier transform of $Cs_2Ag(In_{82.9\%}Tb_{17.1\%})Cl_6$:Bi NCs fitting as a function of R.

To further clarify the occupied crystallographic sites of Tb^{3+} ions in the $Cs_2AgInCl_6$ lattice, Tb L_3-edge EXAFS measurement and analysis for the $Cs_2Ag(In_{82.9\%}Tb_{17.1\%})Cl_6$:Bi NCs were conducted and demonstrated in Figure 1e,f. The EXAFS data obtained was processed in Athena (version 0.9.25) for background, pre-edge line and post-edge line calibrations. Then corresponding Fourier transform (FT) fitting was carried out in Artemis (version 0.9.25). The k^2 weighting, k-range of 3–12 $Å^{-1}$ and R range of 1–3 Å were used for the fitting. The model of Tb^{3+} ions at In^{3+} sites in $Cs_2AgInCl_6$ was used to calculate the simulated scattering paths. The four parameters: coordination number (CN), bond length (R), Debye-Waller factor (σ^2) and E_0 shift (ΔE_0) were fitted without fixed, constrained, or correlated. It can be seen that in Figure 1e,f the spectra were fitted well, with $CN = 5.6 \pm 0.4$, $\Delta E_0 = 4.6 \pm 0.6$ eV, $\sigma^2 = 0.0051 \pm 0.0006$ $Å^2$, and R factor = 0.003, and the details are presented in Table S6. Besides, the fitted bond distance R is 2.65 ± 0.01 Å from Table S6. In the structure of $Cs_2AgTbCl_6$, the bond length of Tb–Cl is 2.66 Å. While in the structure of $Cs_2AgInCl_6$, the bond lengths of In–Cl, Ag–Cl, and Cs–Cl are 2.56, 2.72,

3.74 Å, respectively. Thus the fitted bond length R in the $Cs_2Ag(In_{82.9\%}Tb_{17.1\%})Cl_6$:Bi NCs is closest to the bond length of Tb–Cl. In the FT, the relative decrease in the peak position compared with the actual interatomic distance could be attributed to the photoelectron phase shift.[16] In conclusion, all these results support that the doped Tb^{3+} ions occupied In^{3+} sites.

XPS analyses were also performed to confirm the presence of Tb in the $Cs_2Ag(In_{82.9\%}Tb_{17.1\%})Cl_6$:Bi NCs (Figure S1). The survey XPS spectrum (Figure S1a) showed that both undoped and Tb^{3+} ions doped NCs contained Cs, Ag, In, Cl elements, however, only small amount of Tb can be found in Tb^{3+}-doped NCs. Figure S1b exhibited the two peaks of Tb 3d signals at 1242 and 1277 eV in the 17.1 mol% Tb^{3+}-doped sample readily proving the existence of Tb^{3+} ions in the $Cs_2AgInCl_6$:Bi NCs. Furthermore, comparing the high resolution XPS spectra of In 3d and Ag 3d for Tb^{3+}-doped and undoped NCs (Figure S1c,d), a slight shift to higher binding energy for In^{3+} $3d_{3/2}$ and In^{3+} $3d_{5/2}$ but little variations for Ag^{3+} 3d appeared. The slight shift could be attributed to the lattice expansion after the successful incorporation of Tb^{3+} ions, further confirming the conclusion above that Tb^{3+} ions occupy In^{3+} sites rather than Ag^{+} sites.[9e] TEM images shown in Figure 2 a,c,e,g demonstrated the microstructure of as-prepared undoped and Tb^{3+}-doped $Cs_2AgInCl_6$:Bi NCs. It can be seen that the NCs have similar cubic morphology with the high crystallinity and uniformity. „Dark dots" attached on the NCs could be Ag^0 NCs that have been discussed in previous studies.[5c,14] The selected area electron diffraction (SAED) patterns of corresponding NCs shown in Figure 2 b,d,f,h revealed the presence of (022) and (004) planes of cubic phase, confirming the formation of the consistent perovskite structure. Moreover, as presented in insets of Figure 2 a,c,e,g, the lattice constants increased from 0.37 to 0.39 nm with the increase in Tb^{3+} ions doping concentration, further verifying the lattice expansion consistent with the XRD results above.

Next, we performed first-principles calculations for simulating the difficulty in defect formation and the stabilities of the defect systems of Tb^{3+} ions incorporated into $Cs_2AgInCl_6$ lattice. Figure 3 a showed the relaxed structures of six possible dopant conditions (named A to F) of Tb^{3+}-doped $Cs_2AgInCl_6$, where A–C represented interstitial doping of Tb located previously between nearest Cs–Cs, Cs–Ag and Cs–In atoms, while D–F represented substitution doping of Tb at Cs, Ag, and In site, respectively. The interstitial formation energies (for A–C) were calculated by [Eq. (1)]:

$$E_{for} = E_{tot}(Cs_2AgInCl_6 + Tb) - E_{tot}(Cs_2AgInCl_6) - \mu_{Tb} \quad (1)$$

For substitution situations, the substitution formation energies (for D–F) were calculated by [Eq. (2)]:

$$E_{for} = E_{tot}(Cs_2AgInCl_6 + Tb) - E_{tot}(Cs_2AgInCl_6) + \mu_X - \mu_{Tb} \quad (2)$$

where $E_{tot}(Cs_2AgInCl_6 + Tb)$ and $E_{tot}(Cs_2AgInCl_6)$ represent the total energy of Tb-doped $Cs_2AgInCl_6$ system and undoped $Cs_2AgInCl_6$ crystal, respectively. μ_X (X = Cs, Ag. or In) and μ_{Tb} is the chemical potential of the substitution atom (Cs, Ag. or In) and Tb atom calculated as the corresponding crystal energy per atom. All the formation energies for different dopant conditions are graphically represented in Figure 3 b. Condition A–C have negative formation energies, but with obvious localized twist near the Tb dopant (especially in Condition B), which is mainly caused by the small localized atomic distance between the dopant and the nearest atoms. Condition D (Cs–Tb substitution) has positive formation energies compared with other doping conditions with negative formation energies, indicating an inappropriate solubility of substitution doping of Tb in Cs–Tb substitution. For

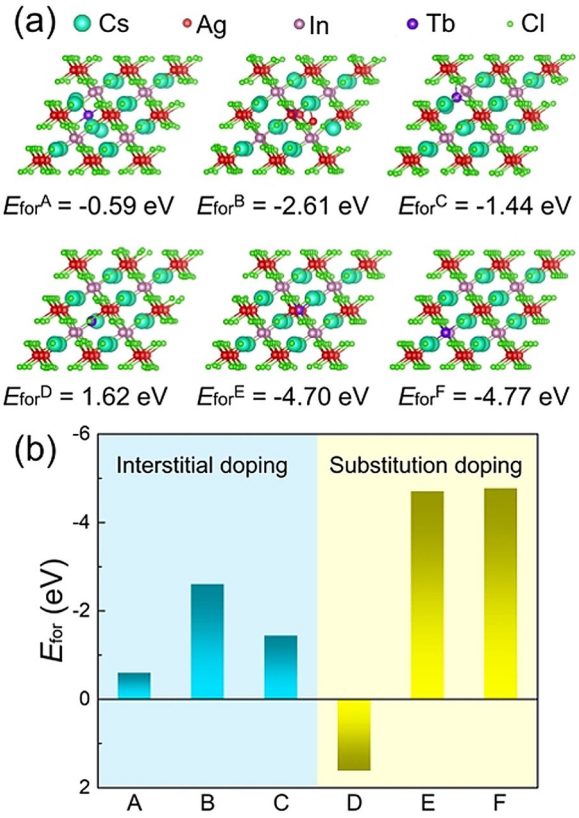

Figure 3. a) Relaxed structures of possible doping conditions of $Cs_2AgInCl_6$ with Tb^{3+} dopant; b) Formation energies for different doping conditions. Condition A–C: interstitial doping of Tb located previously between nearest Cs–Cs, Cs–Ag, and Cs–In atoms, respectively; condition D–F: substitution doping of Tb at Cs, Ag, and In site, respectively.

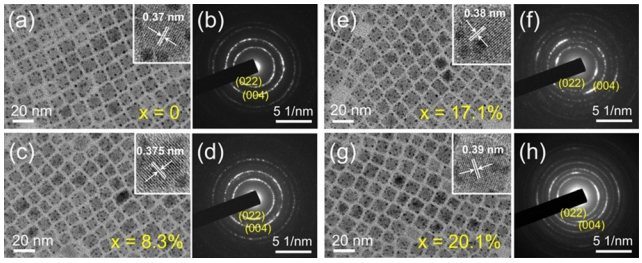

Figure 2. a),c),e),g) TEM and HR-TEM images of Bi doped $Cs_2Ag(In_{1-x}Tb_x)Cl_6$ (x = 0, 8.3%, 17.1%, 20.1%) NCs, respectively. b),d),f),h) Corresponding SAED patterns of Tb^{3+} ions doped $Cs_2AgInCl_6$:Bi NCs.

other substitution doping conditions, the formation energies are lower than those of interstitial doping conditions, and In–Tb substitution (Condition F) has the lowest E_{for} of −4.77 eV, indicating that Ag–Tb and In–Tb substituted environments are more favorable, and Tb substitution at In site was expected to be more easily realized and more feasibly synthesized than Ag site and other interstitial doping in experiments. Besides, the doping of Tb^{3+} ions at In^{3+} ions site could be more favorable as an isoelectronic doping rather than other charged doping site or interstitial doping. In combination of the EXAFS, XPS analyses and the ionic radii comparisons discussed previously, the substitution of Tb atoms at In^{3+} site could be the main occupation for Tb^{3+} ions involved $Cs_2AgInCl_6$.

Bismuth dopant influence on the In-based halide perovskites represented by $Cs_2AgInCl_6$ has been intensely investigated in the previous study.[5b,17] For relative light doping, the dopant system exhibit band gap manipulability[5b] and absorption edge shift. The energy shift is mainly caused by the Bi 6p orbital mixed in the conduction band minimum (CBM) orbital state.[7b] The formation energy for the Bi–Tb binary doping system could be increased due to the relaxation of internal stress comparing with that of Tb doping. But in our study, the Bi contents for samples with different Tb content (up to ca. 20%) are basically consistent (ca. 2%), indicating that the Bi influence on the formation energy and CBM for different samples could be limited and consistent. Therefore, we consider $Cs_2AgIn_{1-x}Bi_xCl_6$ as an established system for the further Tb^{3+} doping, and we focus on the Tb effect on the structural and electronic properties. Thus, we fixed the influence of Bi by neglecting the small amount of Bi in $Cs_2AgInCl_6$, and investigate the Tb influence on the $Cs_2AgIn_{1-x}Bi_xCl_6$ system. The dopant structures with different Tb^{3+} ions doping concentrations were established and fully relaxed with details introduced in the computational method section. For the dopant $Cs_2AgInCl_6$, the Bi dopants remain the lattice vectors and similar geometric structure of pristine $Cs_2AgInCl_6$, and the calculated structural volume increased 0.77% and 1.62% for Tb^{3+} ions doping concentration of 12.5% and 25%, respectively (see Figure S2a), which is in consistent with the variation tendency of experimental measurement. The formation energies for these two dopant structures are 0.77 and 1.81 meV/atom (see Figure S2b), respectively. Such relative formation energies indicate a probability on the formation at room temperature. The calculated absorption coefficients for $Cs_2AgInCl_6$ with different doping concentrations were shown in Figure S3a, as the band edge showed obvious blue shift as the Tb^{3+} ions doping concentration increased, causing enhancement of the optical band gap. Such band gap expansion could also be confirmed in the calculated total density of state (TDOS) shown in Figure S3b, where the CBM moved towards higher energy level when Tb^{3+} ions concentration increased. This could be contributed to the Tb involvement in the $Cs_2AgInCl_6$. The Tb^{3+}-doped $Cs_2AgInCl_6$ could be understood as a solid solution $Cs_2AgIn_{1-x}Tb_xCl_6$ which could be decomposes to two stable double perovskite: $Cs_2AgInCl_6$ and $Cs_2AgTbCl_6$ (both $Fm\bar{3}m$). As the Perdew-Burke-Ernzerhof (PBE) band gap of $Cs_2AgTbCl_6$ (3.63 eV) is larger than that of $Cs_2AgInCl_6$ (1.03 eV), the band gap for the Tb^{3+} ions incorporated $Cs_2AgInCl_6$ could be inevitably enlarged when the Tb^{3+} ions concentration increased. Such band gap variation has already been observed in solid solution perovskite systems with both cation[7b] and anion[18] transmutation. The partial density of state (PDOS) for undoped, 12.5% Tb^{3+}-doped and 25% Tb^{3+}-doped $Cs_2AgInCl_6$ are represented in Figure S3c–e. For Tb^{3+}-doped $Cs_2AgInCl_6$, the upper valence band and valence band maximum (VBM) are mainly contributed by Cl 3p and Ag 3d orbitals analogous to $Cs_2AgInCl_6$, while the CBM state is mainly contributed by In 5s with a small amount of Tb 6s state mixed in. For different Tb^{3+} ions concentrations, the Tb 6s state around CBM increased dramatically when Tb^{3+} ions doping concentration increased. Due to the larger band gap of $Cs_2AgTbCl_6$ comparing with that of $Cs_2AgInCl_6$, such increase of Tb 6s state at CBM would make an enhanced contribution of Tb, causing CBM shift to higher energy level, and eventually increase in band gap.

Having looked deep into the alloying nature of double perovskite NCs, we investigated the luminescence features. Under the excitation of 368 nm, Bi^{3+}-undoped $Cs_2Ag(In_{82.9\%}Tb_{17.1\%})Cl_6$ NCs showed blue emission at 470 nm instead of STEs emission and Bi^{3+}-doped $Cs_2Ag(In_{82.9\%}Tb_{17.1\%})Cl_6$ NCs showed broadband STEs emission at 580 nm, as reported before.[14] We also conduct the fs-TA spectroscopy for Bi^{3+}-doped $Cs_2AgInCl_6$ NCs to verify that the broadband orange emission originates from STEs. A broad photoinduced absorption upon excitation at 365 nm was observed as the direct character of self-trapped excitons (Figure S4).[19] As a comparison, as shown in Figure 4a, $Cs_2Ag(In_{82.9\%}Tb_{17.1\%})Cl_6$ without Bi^{3+} ions exhibited no STEs emission and no characteristic luminescence of Tb^{3+} ions. The optical band gap of $Cs_2Ag(In_{82.9\%}Tb_{17.1\%})Cl_6$ NCs was calculated to be about 4.39 eV from the absorption spectra and corresponding Tauc plot (Figure S5), larger than the corresponding energy from 368 nm illumination. Besides, the absorption spectra of $Cs_2AgInCl_6$ and $Cs_2AgInCl_6$:Bi NCs and the emission of $Cs_2AgInCl_6$ NCs at 290 nm excitation are shown in Figure S6. Although $Cs_2AgInCl_6$ NCs exhibited a broad emission at 290 nm excitation, we could not see the intrinsic emission of $Cs_2AgInCl_6$ NCs in Figure 4a because the low photoluminescence quantum yield of $Cs_2AgInCl_6$ NCs (ca. 1%).[5a] The sharp contrast in the PL intensity between Tb^{3+} ions and $Cs_2AgInCl_6$ NCs at 290 nm excitation made the characteristic emission of Tb^{3+} ions more likely to be excited by its intrinsic excitation band at about 290 nm rather than an energy transfer process. However, after doping a small amount of Bi^{3+} ions, $Cs_2Ag(In_{82.9\%}Tb_{17.1\%})Cl_6$ exhibited both broad emission derived from STEs and sharp emission peaks located at around 490 nm, 550 nm and 620 nm, corresponding to the intrinsic transition of Tb^{3+} ions $^5D_4$-$^7F_6$, $^5D_4$-$^7F_5$ and $^5D_4$-$^7F_3$, respectively with the 368 nm excitation (Figure 4b). The excitation wavelength adjustment also endows the material with the wide range application. Indirectly, the phenomenon suggested that the Tb^{3+} ions emission in Bi doped $Cs_2Ag(In_{1-x}Tb_x)Cl_6$ NCs was not excited directly by 368 nm but excited via an energy transfer channel from the Bi doped $Cs_2Ag(In_{1-x}Tb_x)Cl_6$ NC host to Tb^{3+} ions. Moreover, the emission intensity excited by 368 nm was higher than that by

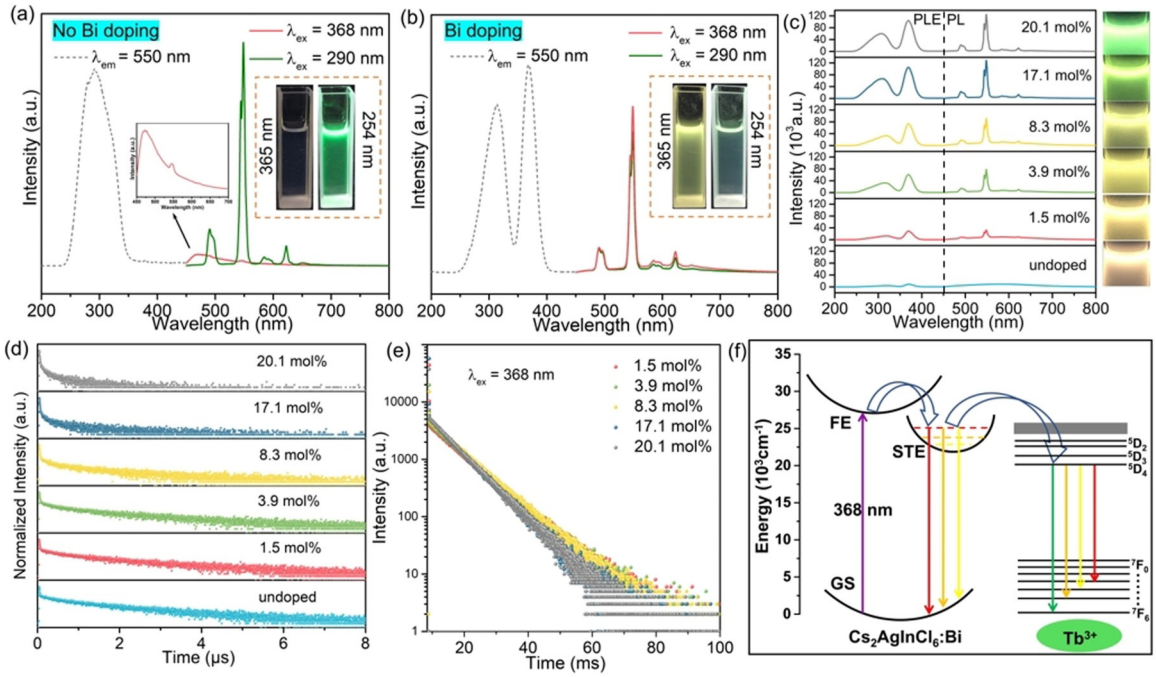

Figure 4. a),b) Emission spectra (right side of spectra, excited by 368 nm and 290 nm) and excitation spectra (left side of spectra, monitored at 550 nm) of undoped and Bi-doped $Cs_2Ag(In_{82.9\%}Tb_{17.1\%})Cl_6$. Insets show an expansion and photographs of the corresponding sample under 254 nm and 365 nm UV irradiation. c) PLE (left side of spectrum, monitored at 550 nm) and PL spectra (right side of spectrum, excited by 368 nm) of Bi doped $Cs_2Ag(In_{1-x}Tb_x)Cl_6$ ($x = 0$, 1.5%, 3.9%, 8.3%, 17.1%, 20.1% NCs. Insets: the photos of the corresponding nanocrystals solution in hexane under the UV-light (365 nm) excitation. d) PL decay curves of STEs emission from corresponding samples monitored at 368 nm excitation and 520 nm emission. e) PL decay dynamics of Tb^{3+} ions emission (550 nm) from Tb^{3+}-doped $Cs_2AgInCl_6$:Bi NCs with different doping contents monitored at 368 nm excitation. f) Energy-level diagram of Tb^{3+} ions doped $Cs_2AgInCl_6$:Bi NCs and the proposed luminescence mechanism.

290 nm (Figure 4b), related to more efficient emission of Tb^{3+} ions through the energy transfer channel than directly via intrinsic excitation band, and the mechanism will be addressed below.

To shed more light on the doping concentration effect on luminescence properties of $Cs_2AgInCl_6$:Bi NCs, the controlled experiment for the samples with different amount of Tb^{3+} ions alloyed was conducted. As presented in Figure 4c and Figure S7, excited at 368 nm (the characteristic excitation of STEs in $Cs_2AgInCl_6$:Bi), the relative intensity of Tb^{3+} ions emission located at 550 nm increased gradually with incremental Tb^{3+} ions added and then decreased from 17.1 mol% Tb^{3+} ions alloyed caused by concentration quenching, which could be the direct existence of the energy transfer in the Bi doped $Cs_2Ag(In_{1-x}Tb_x)Cl_6$ NCs from STEs to Tb^{3+} ions. Surprisingly, the STEs emission in highly Tb^{3+}-doped $Cs_2AgInCl_6$:Bi system almost disappeared and only the strong and sharp lines of Tb^{3+} ions emission existed, indicating that high doping concentration promoted the energy transfer from STEs to Tb^{3+} ions. Simultaneously, as a result of energy transfer, the concentration dependence of Tb^{3+} ions could further tune the emission colors of Bi doped $Cs_2Ag(In_{1-x}Tb_x)Cl_6$ NCs from green to orange as shown in insets of Figure 4c. The absolute photoluminescence quantum yields were 10.1%, 8.1%, 8.0%, 9.2% and 6.6%, respectively, corresponding to the Tb^{3+} concentrations of 0, 3.9, 8.3, 17.1, 20.1 mol%. In addition, to further prove the existence of energy transfer channel, the photoluminescence decay curves for STEs emissions at different Tb^{3+} ions concentrations were measured and exhibited in Figure 4d. The monitored emission wavelength was 520 nm to avoid the interference of Tb^{3+} ions characteristic emission. The photoluminescence decay curves were fitted by triexponential functions with shorter-lived components (τ_1, $\tau_2 < 500$ ns) possibly from deep surface trapping processes[20] and a longer-lived component ($\tau_3 > 500$ ns) corresponding to the STEs lifetime (Table S7). The average lifetime (τ_{ave}) can be calculated with [Eq. (3)],[9f]

$$\tau_{ave} = \sum_i A_i \tau_i \tag{3}$$

The values of average lifetimes (τ_{ave}) were calculated to be 1371.9, 1327.9, 1274.4, 993.7, 577.9, 319.5 ns corresponding to $x = 0$, 1.5, 3.9, 8.3, 17.1, 20.1 mol%, respectively. Thus, the lifetime for STEs decreased with the concentration of Tb^{3+} ions increased (Table S7), further indicating that the improved energy transfer from STEs to Tb^{3+} ions promoted the decay of STEs. The energy transfer efficiency η_T from STEs to Tb^{3+} ions can be obtained by from [Eq. (4)],[21]

$$\eta_T = 1 - \tau_x/\tau_0 \tag{4}$$

where τ_x and τ_0 are the lifetimes of STEs in the presence and absence of Tb^{3+} ions. The values of η_T were estimated to be

3.2%, 7.1%, 27.6%, 57.9% and 76.7% for $x = 1.5$, 3.9, 8.3, 17.1, 20.1 mol%, respectively, revealing that the energy transfer was efficient and the efficiency (η_T) increased with increase in Tb^{3+} ions concentration (Table S7). Besides, the PL decay curves of Bi doped $Cs_2Ag(In_{1-x}Tb_x)Cl_6$ monitored at 550 nm were shown in Figure 4e. The values of Tb^{3+} ions average lifetimes (τ_{ave}) were determined to be 8.9, 8.8, 8.7, 7.6, 7.4 ns at $x = 1.5$, 3.9, 8.3, 17.1, 20.1 mol%, respectively (Table S8). It is obvious that the lifetime of the Tb^{3+} ions decreases gradually as increase in Tb^{3+} ions content which can be ascribed to the concentration quenching effect. Based on the results discussed above, a possible photoluminescence mechanism for Bi doped $Cs_2Ag(In_{1-x}Tb_x)Cl_6$ is proposed and shown in Figure 4f. Under the excitation at 368 nm, the electrons are excited from the ground states into the excited states of $Cs_2AgInCl_6$:Bi NC host and then shift to the self-trapped state through the nonradiative relaxation, emitting broad orange light due to the STEs recombination.[1c,14] Simultaneously, partial energy is transferred to Tb^{3+} ion. Subsequently, electrons at higher level of Tb^{3+} ions are relaxed to the lowest excited level $^5D_4$, and then go back to the ground state, causing the Tb^{3+} ions ($^5D_4 \rightarrow {}^7F_{6\text{-}3}$) characteristic emission. And thus, the emission colors of Bi doped $Cs_2Ag(In_{1-x}Tb_x)Cl_6$ NCs could be continuously tuned from green to orange.

Conclusion

In conclusion, we report the first example of Tb^{3+} ions incorporated $Cs_2AgInCl_6$:Bi NCs to impart and tune the photoluminescence. The structural analysis and the lowest formation energy of −4.77 eV for substitution doping of Tb^{3+} at the In^{3+} site from first-principles calculation demonstrate that Tb^{3+} ions occupy In^{3+} sites in $Cs_2AgInCl_6$ NC hosts. Noted that Bi doping in $Cs_2AgInCl_6$ NCs adjust the excitation of Tb^{3+} ions and allow Tb^{3+} ions to exhibit a characteristic emission under 368 nm excitation, endowing the material with the potential light-emitting diode application under the excitation of commercial near ultraviolet chips. In addition, the introduction of Tb^{3+} ions brought tunable emission from green to orange and we have proposed the energy transfer channel with 368 nm excitation from STEs to Tb^{3+} ions in Bi doped $Cs_2Ag(In_{1-x}Tb_x)Cl_6$ NCs. This work establishes the relationship between the intrinsic emission from lead-free perovskite NCs and the luminescence resulting from lanthanide-ion doping and further promotes the development of new lead-free perovskite NCs for emerging optoelectronic application.

Acknowledgements

This work is supported by the National Natural Science Foundation of China (51961145101, 51972118 and 51722202), Fundamental Research Funds for the Central Universities (FRFTP-18-002C1), Guangdong Provincial Science & Technology Project (2018A050506004) and the Local Innovative and Research Teams Project of Guangdong Pearl River Talents Program (2017BT01X137). This work is also funded by RFBR according to the research project No. 19-52-80003.

Conflict of interest

The authors declare no conflict of interest.

Stichwörter: doping · energy transfer · perovskite nanocrystals · photoluminescence · terbium

[1] a) Q. A. Akkerman, G. Raino, M. V. Kovalenko, L. Manna, *Nat. Mater.* **2018**, *17*, 394 – 405; b) H. Huang, M. I. Bodnarchuk, S. V. Kershaw, M. V. Kovalenko, A. L. Rogach, *ACS Energy Lett.* **2017**, *2*, 2071 – 2083; c) J. Luo, X. Wang, S. Li, J. Liu, Y. Guo, G. Niu, L. Yao, Y. Fu, L. Gao, Q. Dong, C. Zhao, M. Leng, F. Ma, W. Liang, L. Wang, S. Jin, J. Han, L. Zhang, J. Etheridge, J. Wang, Y. Yan, E. H. Sargent, J. Tang, *Nature* **2018**, *563*, 541 – 545.

[2] W. Ning, F. Gao, *Adv. Mater.* **2019**, *31*, 1900326.

[3] T.-B. Song, T. Yokoyama, S. Aramaki, M. G. Kanatzidis, *ACS Energy Lett.* **2017**, *2*, 897 – 903.

[4] a) F. Igbari, Z. K. Wang, L. S. Liao, *Adv. Energy Mater.* **2019**, *9*, 1803150; b) Y. Cai, W. Xie, Y. T. Teng, P. C. Harikesh, B. Ghosh, P. Huck, K. A. Persson, N. Mathews, S. G. Mhaisalkar, M. Sherburne, M. Asta, *Chem. Mater.* **2019**, *31*, 5392 – 5401.

[5] a) F. Locardi, M. Cirignano, D. Baranov, Z. Dang, M. Prato, F. Drago, M. Ferretti, V. Pinchetti, M. Fanciulli, S. Brovelli, L. De Trizio, L. Manna, *J. Am. Chem. Soc.* **2018**, *140*, 12989 – 12995; b) B. Yang, X. Mao, F. Hong, W. Meng, Y. Tang, X. Xia, S. Yang, W. Deng, K. Han, *J. Am. Chem. Soc.* **2018**, *140*, 17001 – 17006; c) Y. Bekenstein, J. C. Dahl, J. Huang, W. T. Osowiecki, J. K. Swabeck, E. M. Chan, P. Yang, A. P. Alivisatos, *Nano Lett.* **2018**, *18*, 3502 – 3508; d) B. Yang, F. Hong, J. Chen, Y. Tang, L. Yang, Y. Sang, X. Xia, J. Guo, H. He, S. Yang, W. Deng, K. Han, *Angew. Chem. Int. Ed.* **2019**, *58*, 2278 – 2283; *Angew. Chem.* **2019**, *131*, 2300 – 2305.

[6] a) K. Z. Du, W. Meng, X. Wang, Y. Yan, D. B. Mitzi, *Angew. Chem. Int. Ed.* **2017**, *56*, 8158 – 8162; *Angew. Chem.* **2017**, *129*, 8270 – 8274; b) A. Karmakar, M. S. Dodd, S. Agnihotri, E. Ravera, V. K. Michaelis, *Chem. Mater.* **2018**, *30*, 8280 – 8290; c) W. Meng, X. Wang, Z. Xiao, J. Wang, D. B. Mitzi, Y. Yan, *J. Phys. Chem. Lett.* **2017**, *8*, 2999 – 3007.

[7] a) R. S. Lamba, P. Basera, S. Bhattacharya, S. Sapra, *J. Phys. Chem. Lett.* **2019**, *10*, 5173 – 5181; b) J. Zhou, X. Rong, P. Zhang, M. S. Molokeev, P. Wei, Q. Liu, X. Zhang, Z. Xia, *Adv. Opt. Mater.* **2019**, *7*, 1801435.

[8] W. J. Mir, T. Sheikh, H. Arfin, Z. Xia, A. Nag, *NPG Asia Mater.* **2020**, *12*, 9.

[9] a) G. Pan, X. Bai, D. Yang, X. Chen, P. Jing, S. Qu, L. Zhang, D. Zhou, J. Zhu, W. Xu, B. Dong, H. Song, *Nano Lett.* **2017**, *17*, 8005 – 8011; b) D. M. Kroupa, J. Y. Roh, T. J. Milstein, S. E. Creutz, D. R. Gamelin, *ACS Energy Lett.* **2018**, *3*, 2390 – 2395; c) D. Zhou, D. Liu, G. Pan, X. Chen, D. Li, W. Xu, X. Bai, H. Song, *Adv. Mater.* **2017**, *29*, 1704149; d) W. J. Mir, Y. Mahor, A. Lohar, M. Jagadeeswararao, S. Das, S. Mahamuni, A. Nag, *Chem. Mater.* **2018**, *30*, 8170 – 8178; e) J. S. Yao, J. Ge, B. N. Han, K. H. Wang, H. B. Yao, H. L. Yu, J. H. Li, B. S. Zhu, J. Z. Song, C. Chen, Q. Zhang, H. B. Zeng, Y. Luo, S. H. Yu, *J. Am. Chem. Soc.* **2018**, *140*, 3626 – 3634; f) C. Luo, W. Li, J. Fu, W. Yang, *Chem. Mater.* **2019**, *31*, 5616 – 5624.

[10] a) W. Lee, S. Hong, S. Kim, *J. Phys. Chem. C* **2019**, *123*, 2665 – 2672; b) Y. Mahor, W. J. Mir, A. Nag, *J. Phys. Chem. C* **2019**, *123*, 15787 – 15793.

[11] N. Chen, T. Cai, W. Li, K. Hills-Kimball, H. Yang, M. Que, Y. Nagaoka, Z. Liu, D. Yang, A. Dong, C. Y. Xu, R. Zia, O. Chen, *ACS Appl. Mater. Interfaces* **2019**, *11*, 16855 – 16863.
[12] S. Li, Q. Hu, J. Luo, T. Jin, J. Liu, J. Li, Z. Tan, Y. Han, Z. Zheng, T. Zhai, H. Song, L. Gao, G. Niu, J. Tang, *Adv. Opt. Mater.* **2019**, *7*, 1901098.
[13] N. Ding, D. Zhou, G. Pan, W. Xu, X. Chen, D. Li, X. Zhang, J. Zhu, Y. Ji, H. Song, *ACS Sustainable Chem. Eng.* **2019**, *7*, 8397 – 8404.
[14] Y. Liu, Y. Jing, J. Zhao, Q. Liu, Z. Xia, *Chem. Mater.* **2019**, *31*, 3333 – 3339.
[15] J. Zhou, Z. Xia, M. S. Molokeev, X. Zhang, D. Peng, Q. Liu, *J. Mater. Chem. A* **2017**, *5*, 15031 – 15037.
[16] J.-P. Ma, Y.-M. Chen, L.-M. Zhang, S.-Q. Guo, J.-D. Liu, H. Li, B.-J. Ye, Z.-Y. Li, Y. Zhou, B.-B. Zhang, O. M. Bakr, J.-Y. Zhang, H.-T. Sun, *J. Mater. Chem. C* **2019**, *7*, 3037 – 3048.
[17] F. Locardi, E. Sartori, J. Buha, J. Zito, M. Prato, V. Pinchetti, M. L. Zaffalon, M. Ferretti, S. Brovelli, I. Infante, L. De Trizio, L. Manna, *ACS Energy Lett.* **2019**, *4*, 1976 – 1982.
[18] J. Zhou, J. Luo, X. Rong, P. Wei, M. S. Molokeev, Y. Huang, J. Zhao, Q. Liu, X. Zhang, J. Tang, Z. Xia, *Adv. Opt. Mater.* **2019**, *7*, 1900139.
[19] a) M. Li, J. Zhou, G. Zhou, M. S. Molokeev, J. Zhao, V. Morad, M. V. Kovalenko, Z. Xia, *Angew. Chem. Int. Ed.* **2019**, *58*, 18670 – 18675; *Angew. Chem.* **2019**, *131*, 18843 – 18848; b) R. Zhang, X. Mao, Y. Yang, S. Yang, W. Zhao, T. Wumaier, D. Wei, W. Deng, K. Han, *Angew. Chem. Int. Ed.* **2019**, *58*, 2725 – 2729; *Angew. Chem.* **2019**, *131*, 2751 – 2755; c) L. Zhou, J. F. Liao, Z. G. Huang, J. H. Wei, X. D. Wang, H. Y. Chen, D. B. Kuang, *Angew. Chem. Int. Ed.* **2019**, *58*, 15435 – 15440; *Angew. Chem.* **2019**, *131*, 15581 – 15586.
[20] A. H. Slavney, T. Hu, A. M. Lindenberg, H. I. Karunadasa, *J. Am. Chem. Soc.* **2016**, *138*, 2138 – 2141.
[21] G. Zhou, X. Jiang, M. S. Molokeev, Z. Lin, J. Zhao, J. Wang, Z. Xia, *Chem. Mater.* **2019**, *31*, 5788 – 5795.

Manuskript erhalten: 28. März 2020
Endgültige Fassung online: 11. Mai 2020

